






Causal impact of tearing mode on zonal flows and local turbulence in the edge of HL-2A plasmas

J.Q. Xu¹, Y.R. Qu², J.C. Li^{3,*}, Z. Lin⁴, J.Q. Dong^{1,5}, X.D. Peng¹,
M. Jiang¹, H.P. Qu¹, Z.H. Huang¹, N. Wu¹, W.C. Wang¹, G.Z. Hao¹,
W. Chen¹, J.Q. Li¹ and M. Xu¹

¹ Southwestern Institute of Physics, PO Box 432, Chengdu 610041, People's Republic of China

² School of Physics, Nankai University, Tianjin 300071, People's Republic of China

³ Department of Earth and Space Sciences, Southern University of Science and Technology, Shenzhen, Guangdong 518055, People's Republic of China

⁴ University of California, Irvine, CA 92697, United States of America

⁵ ENN Science and Technology Development Co. Ltd., Langfang 065001, People's Republic of China

E-mail: jingchunli@pku.edu.cn

Received 2 March 2022, revised 7 June 2022

Accepted for publication 14 June 2022

Published 7 July 2022



Abstract

Direct causality analysis of the multi-scale interactions among macro-scale tearing mode (TM), meso-scale geodesic acoustic mode (GAM) and small-scale turbulence in the edge plasma of the HL-2A tokamak utilizing transfer entropy (TE) method is reported. Experimental results have demonstrated that the $(m/n) = (2/1)$ (with m and n being the poloidal and toroidal mode numbers, respectively) TM modulates the turbulence with the frequency range of $f = 50\text{--}150$ kHz and the GAM mainly modulates that with higher frequencies. The TM has both amplitude and phase modulation on turbulence energy while the GAM has only amplitude regulation effect. TE analyses have shown that both TM and GAM will modulate the turbulence energy during which the impact of the former is of about an order magnitude larger than the latter, whereas the causal effect of TM on particle transport is about twice that of the GAM, which is due to the different causal effects on density and electric field fluctuations caused by TM and GAM, respectively. It is suggested that the magnetic fluctuation strongly modulates the Reynolds stress which serves as a mediator, leading to a cooperative interaction between TM and GAM in the edge of tokamak plasmas.

Keywords: tearing mode, GAM, modulation, transfer entropy

(Some figures may appear in colour only in the online journal)

1. Introduction

It is widely known that the tokamak plasma is a highly complex nonlinear system which consists of large-scale magnetohydrodynamic (MHD) modes and drift-wave microinstabilities [1–3]. Besides, both experiments and simulations have demonstrated that meso-scale zonal flows (ZFs) [4] including the low frequency ZFs [5] and the high

frequency branch geodesic acoustic modes (GAMs) [6] will be excited in the case of fully developed drift-wave turbulence through nonlinear three-wave interactions which can regulate or suppress the turbulent transport [7–9]. From this perspective, it is of great importance to clarify the underlying physics of the multi-scale interactions among MHD mode such as tearing modes (TMs) [10] and neoclassical tearing modes (NTMs) [11], ZFs and ambient broadband fluctuations in order to give a full understanding of the nature of plasma

* Author to whom any correspondence should be addressed.

turbulence as well as the transport, hence providing potential controlling mechanisms of plasma performance in future fusion devices such as ITER [12].

Over the last decade, much effort has been made in identifying the background microturbulence in the presence of TMs or NTMs, where the latter are commonly characterized by magnetic islands (MIs) [13] and the former is driven by various kinds of gradients which are significantly altered by the TMs/NTMs or a modification of the equilibrium profiles due to their presence [14]. In other words, the microinstabilities increase outside the MI and decrease inside the MI following the gradients, therefore it is strongly suggested that the evolutions of turbulence and MI are strongly coupled [15]. Experimental observations of the interactions between turbulent fluctuations and MIs have been extensively studied and it has been found that the multi-scale interaction of MIs with turbulence is important in transport regulation in plasmas core and is suspected to play a key role during the low-to-high confinement transition. For example, the first measurements of localized reduction of turbulent density fluctuations [16] as well as the reduction of cross-field transport at the O -point of $(m/n) = (2/1)$ NTMs [17] is reported for DIII-D experiments. The interaction between MI and turbulence via coupling between the electron temperature gradient, the turbulence and the poloidal flow in KSTAR is clarified [18] and the modulation effects on microturbulence by the TMs are demonstrated by the correlation between turbulence envelope and magnetic fluctuations on EAST tokamak [19]. The influence of magnetic topology on radial electric fields, turbulence and confinement has also been reported previously. Estrada *et al* has investigated the effect of $(m, n) = (2, 3)$ MIs on plasma flow and turbulence at the TJ-II stellarator, showing that the transport barriers (TBs) was linked with MIs [20]. Ida *et al* has measured the plasma flow across the $(n, m) = (1, 1)$ MI in the large helical device (LHD) plasmas, indicating that poloidal flow was damped inside the MI and the flow shear was reduced if the width of MI became larger, which has provided a possible explanation of the link between the position of TB and the location of low order rational surface [21]. In addition, dedicated experiments carried out on the HL-2A tokamak have indicated that both the perpendicular flow and the density fluctuation level are modulated by the naturally rotating TM near the island boundary [22] and provided the first evidence that the turbulence modulation occurs only when the island width exceeds a certain threshold value [23]. On the theoretical side, gyrokinetic simulations generally indicate that the MI will modulate the background turbulence which is mainly determined by ion temperature gradient mode [24, 25] in the plasma core and multi-scale interactions causing the appearance of MI in quasi-steady turbulent state including ZFs and GAM is firstly presented by two-fluid simulations [26]. Although these experimental observations and simulations have suggested the influence of MIs on turbulence, a clear understanding of the nature of the *causal* impact of MIs on turbulence transport is still missing up to now mainly due to two reasons: one is that the experimental data which measures the evolutions of MIs, ZFs and transport simultaneously are extremely limited; the other is the lack of an appropriate

causality analysis method as the conventional linear analysis techniques such as correlations may lead to confusing or even erroneous conclusions regarding causality, which is referred to as the well-known adage ‘*correlation does not imply causation*’ (see reference [27]). Therefore, the causal influence of MIs on ZFs and turbulence must be carefully dealt with, which is the main objective of the present paper.

In this work, we present the first causality analysis of the multi-scale interactions among TM, GAM and turbulent transport based on the transfer entropy (TE) technique. All the fluctuations were measured simultaneously in the edge plasma of the HL-2A tokamak using Langmuir probe (LP) arrays and the causal relations among these different spatial scale fluctuations are clearly identified. The rest of the paper is organized as follows. The experimental setup and analysis techniques are presented in section 2. The experimental results of the impact of TM on GAM and local turbulence are demonstrated in section 3. Finally, the conclusions are drawn in section 4.

2. Experimental setup and analysis techniques

The experiments were performed in the ohmically heated deuterium plasmas in the HL-2A tokamak (major radius $R = 1.65$ m and plasma minor radius $a \approx 0.32$ m) [28] with plasma current $I_p \sim 150$ kA, toroidal magnetic field $B_T \sim 1.3$ T and central line-averaged density $\bar{n}_e \approx 0.8\text{--}1.2 \times 10^{19} \text{ m}^{-3}$. The fluctuations have been measured in the plasma boundary region using a fast reciprocating LP system located at the middle plane of the device which has been successfully used in the investigations of the physics of sheared flows [29] and L–I–H transitions [30]. In this paper, the analysis methods used to characterize the spectral feature of the multi-scale interaction are mainly bispectrum, envelope analysis and TE techniques. Here we only give brief descriptions of TE technique. The TE introduced in the field of information theory [31] that was recently applied in the context of fusion plasmas for the first time in order to quantify the ‘*causal*’ impact of one turbulent variable on another [32]. The TE is a measure of the causal relation between two time series which differs from the correlation in the sense that it is directional and allows the identification of an information flow between correlated sequences. This nonlinear technique measures the ‘*information transfer*’ between two signals, is directional, and uses all the information available in the two signals regardless of amplitude or sign.

Considering simultaneously measured signals X and Y yielding discretely sampled time series data x_i and y_j that quantifies the number of bits by which the prediction of the next sample of signal X can be improved by using the time history of not only the signal X itself, but also that of signal Y . A simplified version of the TE can be evaluated as follows

$$T_{Y \rightarrow X}(k) = \sum p(x_{n+1}, x_{n-k}, y_{n-k}) \times \log_2 \frac{p(x_{n+1} | x_{n-k}, y_{n-k})}{p(x_{n+1} | x_{n-k})}. \quad (1)$$

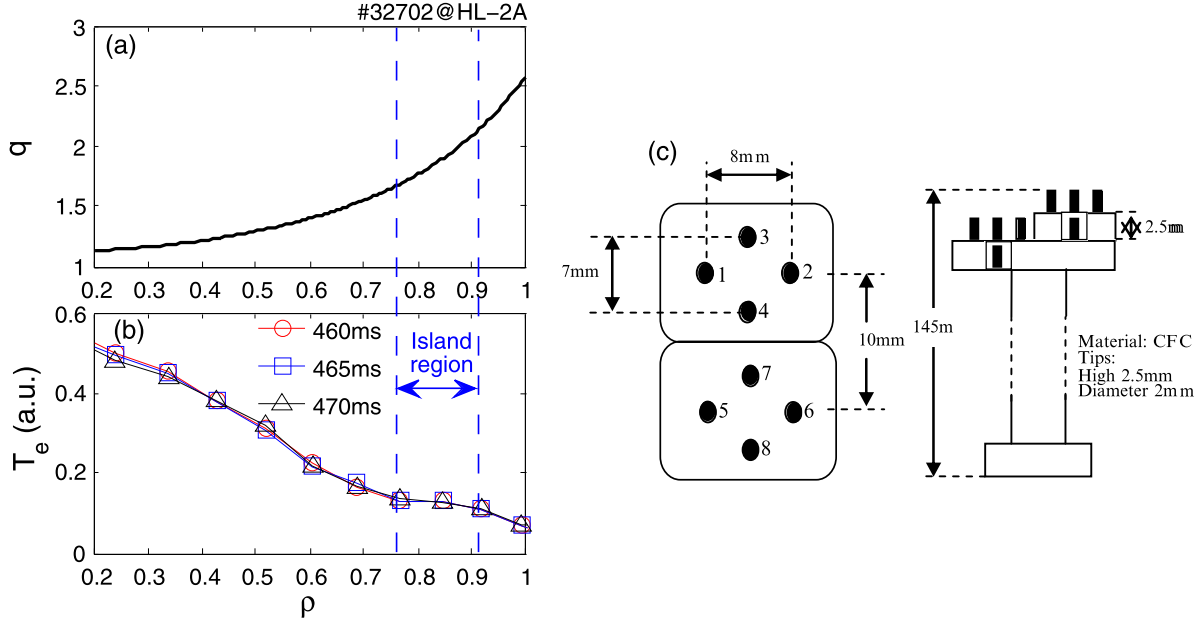


Figure 1. Profiles of (a) safety factor q and (b) electron temperature T_e . The island region of the $(m/n) = (2/1)$ TM is indicated by the vertical dashed lines. (c) Configurations of the fast reciprocating probe array.

Here, $p(x|y) = p(x, y)/p(y)$ is the probability distribution of x conditional on y . The probability distributions $p(a, b, c, \dots)$ are constructed using m bins for each argument, i.e. the object $p(a, b, c, \dots)$ has m^d bins, where d is the dimension of p . The sum in equation runs over the corresponding discrete bins. Here n is the length of the signal and k is the time-delay embedding vector which can be converted to ‘time lag’ by multiplying the sampling time, $\Delta\tau = k/f_s$ [33]. The construction of the probability distributions is done using ‘course graining’, i.e. a low number of bins (here $m = 2$ or 3), to obtain statistically significant results. The value of the TE T , expressed in bits, can be compared with the total bit range, $\log_2 m$ which equals to the maximum possible value of T , to help decide whether the TE is significant or not. The TE is the information flow which measures the degree of decrease of uncertainty in prediction one variable with the help of another, i.e., it is the increase of the precision in predicting signals based on existing observations. For more details on the technique, please refer to [32]. Calculating the TE as a function time delay can truly and accurately reflect the time scale of the maximum effect of one variable on another. In a modulation system, the effect of one physical quantity on another generally has a certain time delay. The TE can reveal the real time delay when the greatest information flow as well as the causal impact of TM/GAM on turbulence reaches maximum in the present study. The physical meaning of TE waveforms can be inferred from the comparisons between the TE waveforms and the cross correlation functions or cross spectrums. It is generally observed that the maximum values of cross correlation coefficient and TE occur at almost the same time lag, suggesting that the TE can not only reflect the maximum coherence but also the maximum causal effect as well. The modulation effect is verified from the periodic feature of the TE waveforms at a certain frequency, as characterized by the cross spectrums in the present paper.

3. Experimental results

The MI region is depicted in figure 1, in which figures 1(a) and (b) show the profiles of safety factor q computed by the equilibrium and reconstruction fitting code and the T_e measured by electron cyclotron emission system [34], respectively. The MI mainly exists in the region of about $\rho = r/a \approx 0.76$ – 0.91 , which is identified to be an $(m/n) = (2/1)$ TM [22]. The position of the LPs is located at around $\rho \approx 0.92$, near to the MI boundary. To make the required edge plasma measurements, a probe array with two steps located at the outer mid-plane was inserted into the plasma to measure the fluctuations, as shown by the sketch in figure 1(c). The data from LP are digitized at the sampling frequency $f_s = 1$ MHz with 12 bit accuracy. The pins numbered by (1, 2) and (5, 6) are pairs of standard double probes used to sample the ion saturation current, $I_{s1(2)} = (V_{1(5)} - V_{2(6)})/R_{\text{sample}}$ with R_{sample} being the sampling resistance. Pins numbered by (3, 4) and (7, 8) are used for detecting floating potentials (ϕ_f), from which the radial electric field E_r can be deduced from the two radially separated pins as $E_r = (\phi_{f4} - \phi_{f7})/\Delta r$ while the poloidal electric field E_θ is estimated as $E_{\theta 1(2)} = (\phi_{f3(7)} - \phi_{f4(8)})/\Delta\theta$, respectively. The distances are $\Delta r = 2.5$ mm and $\Delta\theta = 7.0$ mm, respectively. The local electron temperature and density are thus calculated as $T_{e1} = [V_2 - (\phi_{f3} + \phi_{f4})/2]/\ln 2$ and $n_{e1} = 2I_{s1}/[eA_{\text{eff}}(kT_e/m_i)^{0.5}]$, where A_{eff} , k and m_i stand for the effective area of 10.0 mm², the Boltzmann coefficient and the ion mass, respectively. The radial particle flux and the electrostatic component of the Reynolds stress (RS) have been computed in the plasma boundary region as $\Gamma_r = \langle \tilde{r}_r \rangle = \langle \tilde{n}_e \tilde{E}_\theta \rangle / B_T$ and $\Pi_{r\theta} = \langle \tilde{v}_r \tilde{v}_\theta \rangle = -\langle \tilde{E}_r \tilde{E}_\theta \rangle / B_T^2$, where the bracket donates the ensemble average [35]. The magnitudes of RS and its radial gradient are of the order 10^5 m² s⁻² and 10^7 m s⁻² in the

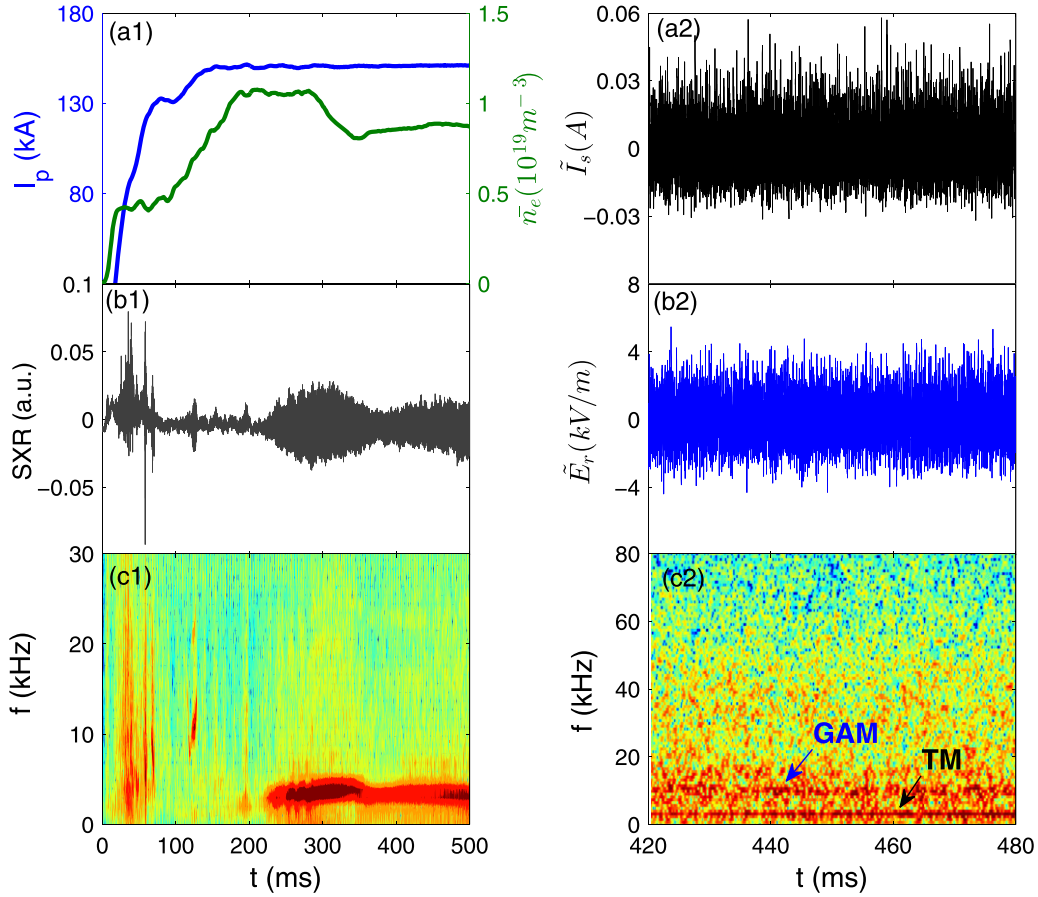


Figure 2. Left panel: (a1) plasma current I_p and line-averaged density \bar{n}_e , (b1) SXR signal and (c1) spectrogram of SXR signal. Right panel: (a2) ion saturation current fluctuation \tilde{I}_s , (b2) radial electric field fluctuation \tilde{E}_r and (c2) spectrogram of \tilde{E}_r measured by the probe.

present experiment, which are suggested to be the main driving force of the GAMs. The radial correlation lengths of GAM and turbulence using two-point technique [36] are estimated to be about $L_{r,GAM} \sim 0.7$ cm and $L_{r,turb} \sim 0.4$ cm while the poloidal correlations lengths are about $L_{\theta,GAM} \sim 6.3$ cm and $L_{\theta,turb} \sim 2.6$ cm, respectively. Based on the above calculations, it is strongly believed that the both the probe pins in the poloidal and radial directions are measuring the single GAM activity or turbulence eddy simultaneously, i.e., the fluctuations are measured within the correlation volume of them and the spatial differences as well as the cross phase induced by them can be neglected. Therefore, we can directly measure the characteristics of turbulence at the MI boundary and the influence of phase shift caused by the spatial differences on the results is excluded effectively. It should be noted that the modulation of AT by TM may depend on the radial location. Experimental results have shown that if the MI width is large enough, the plasma flow inside the MI will be reversed and the dominant drift instability will change as the gradient changes tremendously inside and outside the MI. Hence, the causal influence among poloidal flow, TM and background turbulence may vary significantly depending on both the radial location and the width of MI. However, our probe is only limited to measure the fluctuations outside the boundary of MI at present and the measurement at other positions will be carried out in the future work.

3.1. Spectral features of the interactions between TM, GAM and turbulence

The discharge waveforms and physical quantities measured by probes are shown in figure 2. Figures 2(a1) and (b1) show the discharge parameters of I_p , \bar{n}_e and the soft x-ray (SXR) signal at radial position $r = 29.6$ cm corresponding to normalized radius of $\rho \approx 0.91$ while its frequency spectrum is illustrated in figure 2(c1) in which strong TM is observed. Although there is some difference between the positions of SXR and LP, it is strongly suggested that the phase shift induced by the spatial difference is rather small due to the global nature of the TM eigenmode structure. Figures 2(a2) and (b2) demonstrate the ion saturation current fluctuation \tilde{I}_s (proportional to density fluctuation [37]) and the radial electric field fluctuation \tilde{E}_r measured by the probe, corresponding to a quasi-steady state as donated by the shadow region in the left panel. The spectrogram of \tilde{E}_r is shown in figure 2(c2) in which both an oscillation around the TM frequency $f \approx 3.4$ kHz and a coherent mode around $f \approx 10.2$ kHz are clearly observed simultaneously. The latter is GAM which has been identified by both probes [38] and correlation Doppler reflectometry [39]. These results have suggested that the multi-scale interactions can be evaluated by the probe data.

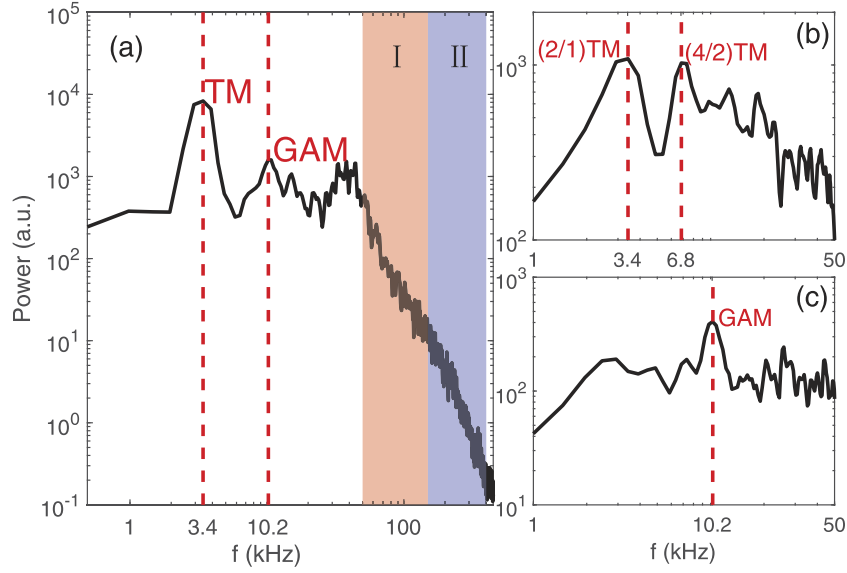


Figure 3. Power spectrum of (a) \tilde{E}_r , (b) \tilde{I}_s envelope in the frequency range of $f = 50\text{--}150$ kHz and (c) \tilde{I}_s envelope in the frequency range of $f = 150\text{--}400$ kHz.

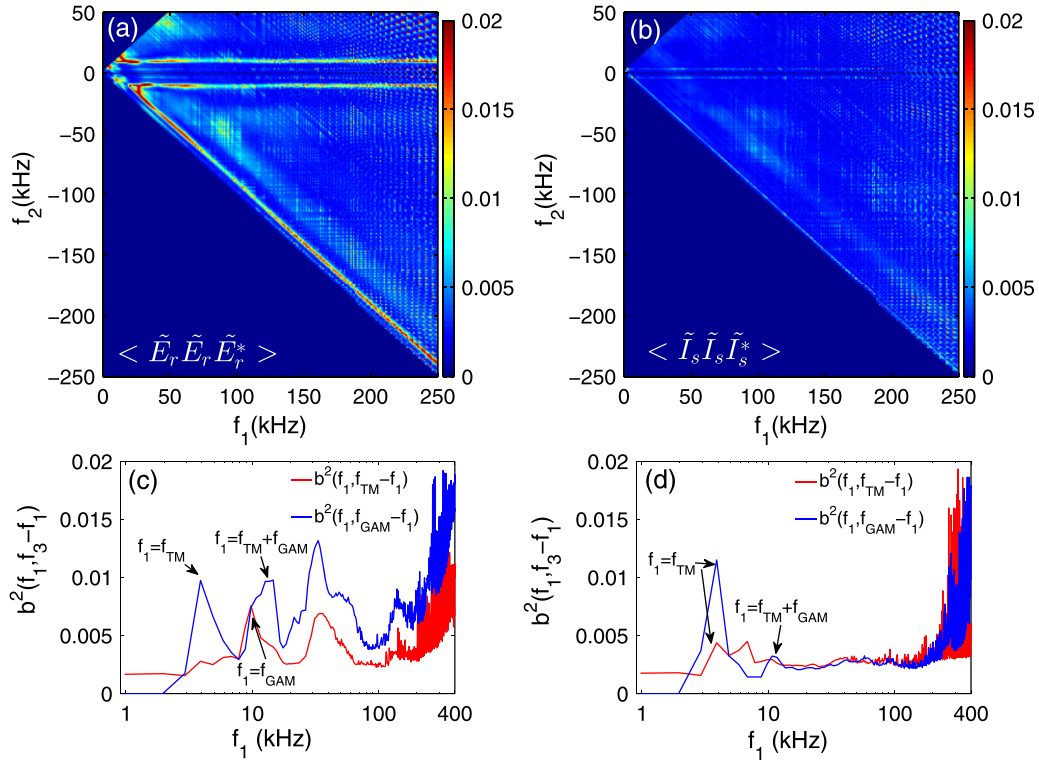


Figure 4. Wavelet autobicoherence of (a) \tilde{E}_r and (b) \tilde{I}_s . The corresponding slices of the bispectrum at the TM (red) and GAM (blue) frequencies are shown by (c) and (d), respectively.

For further investigations of the modulation and coupling relationship between TM, GAM and turbulence, a variety of spectral analysis methods were used. Figure 3 shows the power spectrum of \tilde{E}_r and bandpass filtered envelopes of \tilde{I}_s . Here the envelope based on the analytic signal approach is composed of a real signal of finite energy which is Fourier transformable and band-limited and the Hilbert transform of the original real signal. For a real signal $S_r(t)$ the corresponding analytic signal is

defined as $S(t) = S_r(t) + i\hat{S}_r(t)$ where $\hat{S}_r(t)$ is the Hilbert transform of $S_r(t)$ as $\hat{S}_r(t) = \frac{1}{\pi} \int_{-\infty}^{+\infty} \frac{S_r(\tau)}{t-\tau} d\tau$. The envelope is then defined as the modulus of the analytic signal. The information on the nonlinear interaction between the GAM and turbulence is embodied in the envelopes. Thus, the modulation interaction can be identified by using correlation techniques between the envelopes of bandpass filtered fluctuations. In figure 3(a), there are two prominent peaks at 3.4 kHz and 10.2 kHz, repre-

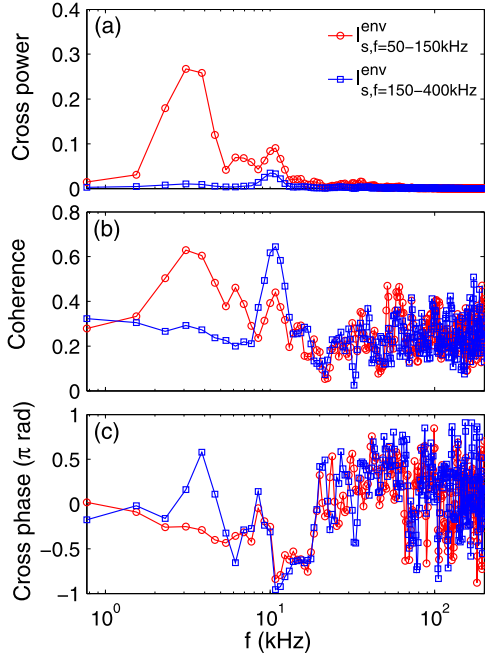


Figure 5. (a) Cross power, (b) coherence and (c) cross phase between \tilde{E}_r and envelopes of bandpass filtered \tilde{I}_s .

sending TM and GAM, respectively. The density fluctuation is filtered and enveloped before the spectrum is obtained in order to explore the modulation interaction among TM, GAM and high frequency turbulence. The frequency ranges have been carefully selected so as to investigate the effect of one mode while exclude the other simultaneously in order to reveal the modulation of TM and GAM on turbulence distinctly. This is achieved by examining the power spectrum of the envelope of density fluctuation, as shown in figures 3(b) and (c), in which the auto-power spectrum has only clear peaks at the TM and GAM frequencies and the selected frequency bands do not overlap. The spectrum of the \tilde{I}_s envelope in the frequency range $f = 50\text{--}150\text{ kHz}$ corresponding to region I is shown figure 3(b). The $(m/n) = (2/1)$ TM and its second harmonic wave, $(m/n) = 4/2$ TM are noteworthy, indicating that there is a strong regulation of TM on the turbulence energy. Figure 3(c) shows the result in the frequency range II ($f = 150\text{--}400\text{ kHz}$). The peak around 10.2 kHz represents the GAM, showing the modulation of GAM on turbulence within higher frequencies. The comparison between figures 3(b) and (c) is especially interesting, which strongly suggests that the effects of TM and GAM on turbulence are within different spatial scales. The frequency range of TM affecting turbulence is lower than that of GAM, which has never been discovered in other studies.

The wavelet bispectrum [40] of radial electric field fluctuation is demonstrated in figure 4, which is defined as $B^w(a_1, a_2) = \int W_f^*(a_1, \tau) W_f(a_1, \tau) W_f(a_2, \tau) d\tau$ where the frequency sum rule is satisfied, $1/a = 1/a_1 + 1/a_2$. The wavelet transform of a function $f(t)$ is given by $W_f(a, \tau) = \int f(t) \Psi_a(t - \tau) dt$ and $*$ denotes the complex conjugate. Here Ψ_a is wavelet kernel and a is the wavelet scale, respectively.

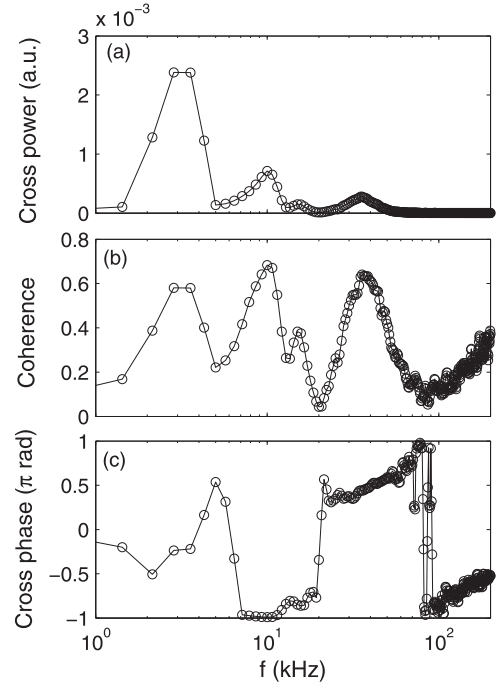


Figure 6. (a) Cross power, (b) cross coherence and (c) cross phase between \tilde{E}_r and bandpass filtered \tilde{I}_s in the frequency domain.

The squared wavelet bicoherence is the normalized squared bispectrum, $[b^w(a_1, a_2)]^2 = \frac{|B^w(a_1, a_2)|^2}{\left[\int |W_f(a_1, \tau) W_f(a_2, \tau)|^2 d\tau \right] \left[\int |W_f(a, \tau)|^2 d\tau \right]}$ and the summed bicoherence is defined as $[b^w(a)]^2 = \sum [b^w(a_1, a_2)]^2$ where the sum is taken over all a_1 and a_2 which satisfies the frequency sum rule. Although the GAM ZF will show an acceleration in its energy flow in case of time series analysis, we believe it is not important as the experiments here are of quasi-steady state nature which is an idealization of the real steady state, during which the rate of energy transferred from background turbulence to GAMs balances the damping rate of the latter. Figure 4(a) shows the contour plot of auto-bicoherence $\hat{b}_{\tilde{E}_r \tilde{E}_r \tilde{E}_r^*}^2(f_1, f_2)$. From the figure, significant nonlinear coupling is observed at the GAM frequency, $f_2 = \pm 10.2\text{ kHz}$ and $f_1 + f_2 = f_3 = 10.2\text{ kHz}$. The auto-bicoherence in terms of $\hat{b}_{\tilde{I}_s \tilde{I}_s \tilde{I}_s^*}^2(f_1, f_2)$ is also plotted for a comparison, as shown in figure 4(b), where only weak nonlinear coupling between ambient turbulence (AT) and TM is found but it is almost invisible at the GAM frequency. Figure 4(c) illustrates the summed auto-bicoherence of \tilde{E}_r and \tilde{I}_s , from which it can be seen that although a small peak around the TM frequency is observed in both curves, its magnitude is comparable to or smaller than that of at other frequencies. Besides, the value of $\sum \hat{b}_{\tilde{I}_s \tilde{I}_s \tilde{I}_s^*}^2(f)$ is much smaller than that of $\sum \hat{b}_{\tilde{E}_r \tilde{E}_r \tilde{E}_r^*}^2(f)$ at the GAM frequency. This fact clearly demonstrates that the auto-bicoherence of density fluctuations is not a useful measure for detecting the nonlinear interaction between the GAM and AT, which is in contrast to the auto-bicoherence of radial electric fluctuations. More importantly, it is strongly suggested that the TM hardly satisfies the frequency sum rule, i.e., the TM is resulted from magnetic reconnection rather than

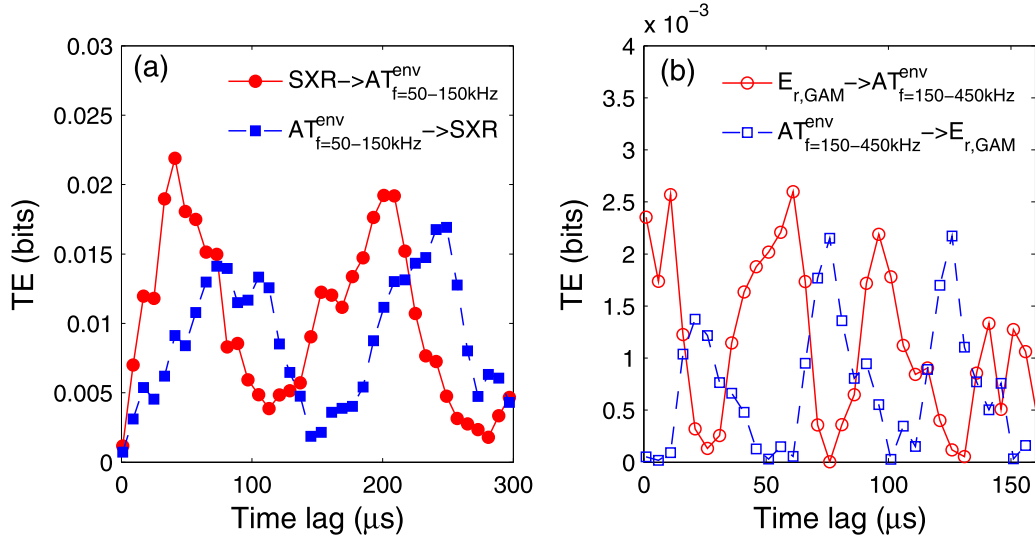


Figure 7. TE as a function of time lag between (a) TM and AT energy of $f = 50\text{--}150\text{ kHz}$ and (b) $\tilde{E}_{r,\text{GAM}}$ and AT energy of $f = 150\text{--}400\text{ kHz}$.

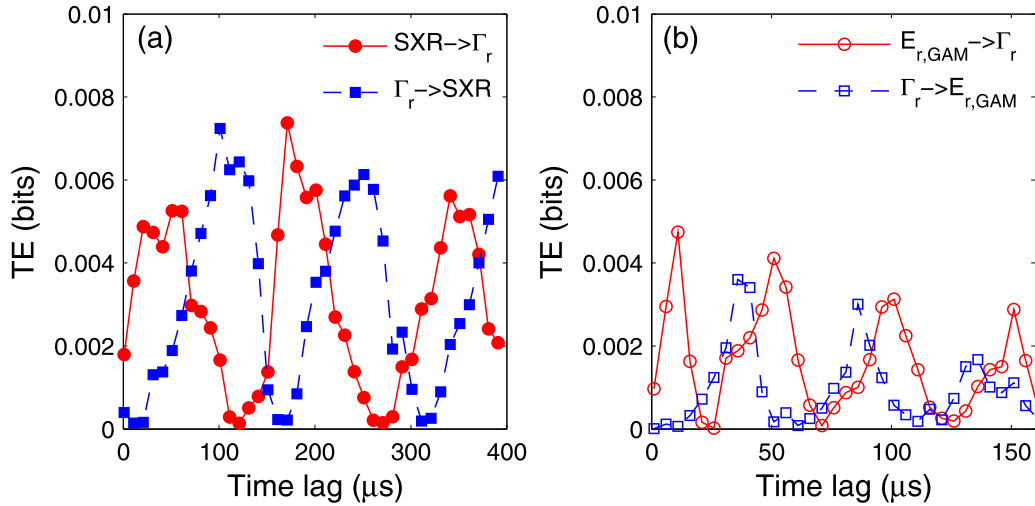


Figure 8. Causal relation as a function of time lag between (a) TM and Γ_r and (b) GAM and Γ_r .

the nonlinear three-wave coupling in the present study. The existence of TM will modulate the turbulence but its generation is independent of the three-wave interaction. This result is different than the very recent experimental observation where the NTMs are seeded by the nonlinear behavior of turbulence as reported in DIII-D [41] and KSTAR [42], namely, the NTMs there are excited by nonlinear three-wave interaction of drift-wave microturbulence.

The coexistence of TM and GAM suggests that both these two oscillatory flows and turbulence have nonlinear interactions. In order to give a clear understanding of the interaction among TM, GAM and background turbulence, the bispectrum are plotted along the oblique lines at fixed frequencies of $f_3 = f_1 + f_2 = f_{\text{TM}}$ and $f_3 = f_1 + f_2 = f_{\text{GAM}}$ in figures 4(c) and (d). In figure 4(c), in the curve $f_3 = f_{\text{TM}}$ the peak at frequency $f_1 = f_{\text{GAM}}$ corresponds to the strong interaction between the GAM ($f_1 = f_{\text{GAM}}$), background turbulence

($f_2 = -f_{\text{GAM}} + f_{\text{TM}}$) and TM ($f_1 + f_2 = f_{\text{TM}}$), while the second peak at $f_1 \sim 35\text{ kHz}$ suggests the nonlinear interactions between turbulence with different frequencies. On the other hand, in the curve $f_3 = f_{\text{GAM}}$, two obvious peaks at $f_1 = f_{\text{TM}}$ and $f_1 = f_{\text{GAM}} + f_{\text{TM}}$ are found. The first peak indicates the interaction among TM ($f_1 = f_{\text{TM}}$), turbulence ($f_2 = f_{\text{GAM}} - f_{\text{TM}}$) and GAM ($f_1 + f_2 = f_{\text{GAM}}$) while the second one donates the coupling among turbulence ($f_1 = f_{\text{GAM}} + f_{\text{TM}}$), TM ($f_2 = f_{\text{TM}}$) and GAM ($f_1 + f_2 = f_{\text{GAM}}$), respectively. The third peak at $f_1 \sim 35\text{ kHz}$ is the turbulence peak which suggests the nonlinear interactions of the AT. Similar features are also discovered for the bicoherence of \tilde{I}_s in figure 4(d) in addition to the fact that weak nonlinear interaction is found at the GAM frequency for fixed $f_3 = f_{\text{TM}}$, which can also be verified through figure 4(b). The above results also suggest the different modulation effects of TM and GAM on potential and density fluctuations, which will be investigated in detail in the future.

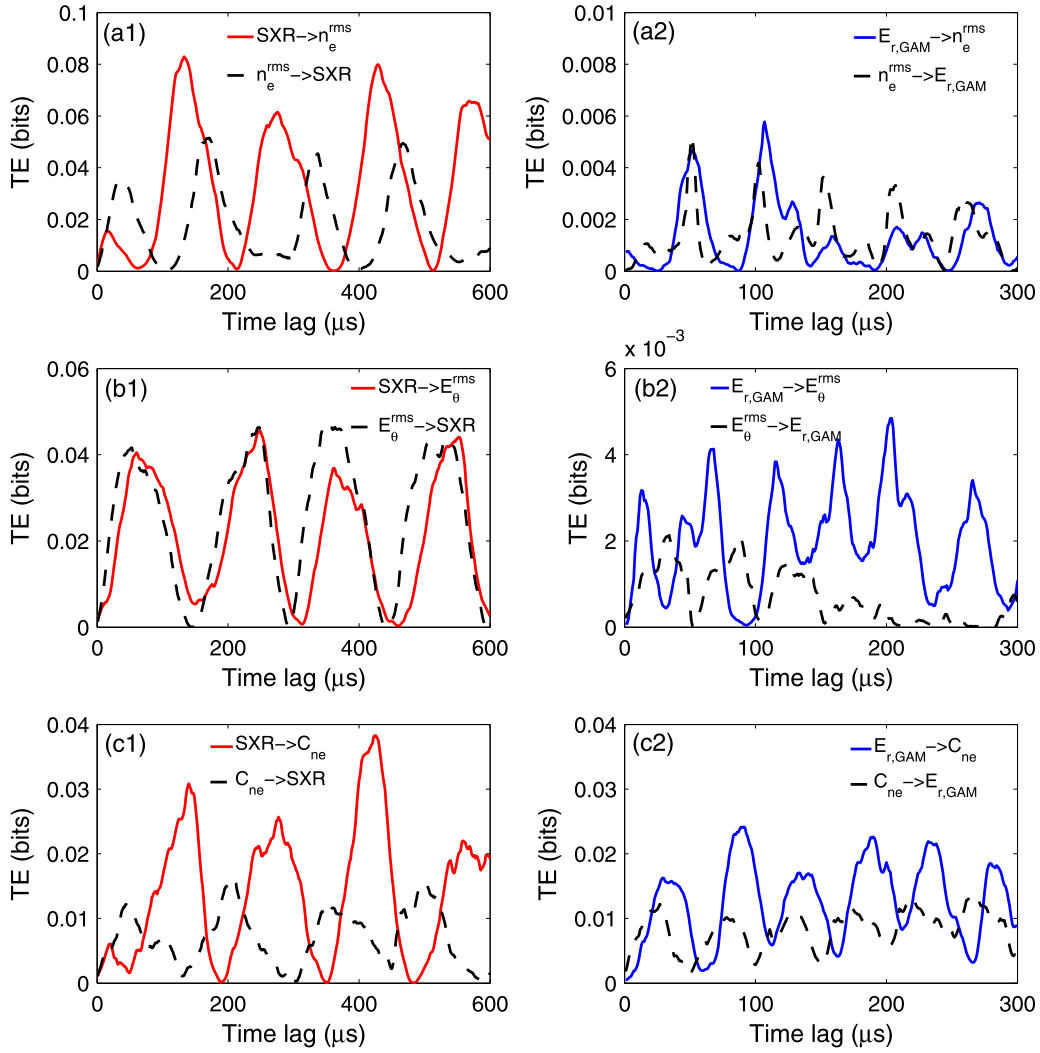


Figure 9. Causal impact of TM and GAM on each component of particle flux in terms of the RMS of density fluctuation (n_e^{rms}), poloidal electric field fluctuations (E_θ^{rms}) and the coherence (C_{ne}) between them. (a1)–(c1) are the results for TM and turbulence while (a2)–(c2) are that for GAM, respectively.

It is also necessary to identify the modulation effect of TM and GAM on turbulence energy, which can be achieved by the cross coherence between \tilde{E}_r and the envelopes of bandpass filtered \tilde{I}_s . The corresponding results are shown in figure 5. Significant peaks at the frequencies of TMs and GAM are discovered in both the cross power and coherence for the \tilde{I}_s envelope in the frequency range of $f = 50\text{--}150\text{ kHz}$, indicating that the modulation of the turbulence envelope correlates strongly with the TM and GAM during which the effect of the former is much stronger than that of the latter, as can be inferred from figures 5(a) and (b). For the case of $f = 150\text{--}400\text{ kHz}$, the amplitudes of cross power and coherence at the GAM frequency is much larger than that at the TM frequency, indicating that the modulation of turbulence is mainly resulted from the GAM oscillation. The cross phases at the TM and GAM frequencies are quite different, i.e., around $-\pi/4$ or $\pi/6$ for TM whereas about $-\pi$ for GAM, respectively, as shown in figure 5(c). This indicates that the TM has both amplitude and phase modulations whereas the GAM has only amplitude

modulation effect on turbulence, respectively. It is noted that although both the TM and GAM will modulate the turbulence regardless of the frequency ranges, the effect of the one can be neglected once the influence of the other is obviously stronger. From these analyses above, it is believed that the selection of the frequency ranges is appropriate in distinguishing the causal influences of TM and GAM on turbulence with different spatial scales.

The correlation between \tilde{E}_r and bandpass filtered \tilde{I}_s is presented in figure 6 in order to determine the relationship in the frequency domain, where the frequency range of \tilde{I}_s is $f = 50\text{--}400\text{ kHz}$. In both figures 6(a) and (b), two peaks at the frequencies corresponding to TM and GAM are observed, implying the modulation of TM and GAM on background fluctuation simultaneously. The cross phase plotted in figure 6(c) shows that the phase shifts are around $-\pi/4$ and $-\pi$ at the TM and GAM frequencies, suggesting that the TM has amplitude as well as phase regulations whereas the GAM has only amplitude modulation effect on turbulence, respectively.

3.2. Causal relations of multi-scale interactions among TM, GAM and transport

The multi-scale interactions are determined by the TE calculations, which could provide the transfer of entropy, or information flow among different spatial scales. Figure 7 shows the TE between TM/GAM fluctuation and envelope of \tilde{I}_s . Here the TM fluctuation is donated by the SXR signal and the GAM oscillation, donated by $\tilde{E}_{r,GAM}$, is extracted by bandpass filtered \tilde{E}_r in the frequency range of $f = 7-12$ kHz, respectively. Besides, the frequency ranges of \tilde{I}_s in figures 7(a) and (b) are different due to the reason that TM and GAM act on different scales, as previously stated in figure 3. In both situations, the TE behaves periodically with the periods coinciding with that of TM and GAM, respectively. This indicates that the influence of both large and meso-scale modes on AT is periodic in addition to the fact that the effect of TM is of about an order magnitude larger than that of the GAM. More significantly, this shows that the causal influence is mutual instead of unidirectional. Besides, the TM acts on turbulence energy on a faster time scale, whereas the latter acts back on a longer time scale, which can be inferred from the difference in the time delay of the peaks. Similar trends are also found in the causal relation between GAM and turbulence and the modulation period of GAM is shorter than that the case of TM due to the higher frequency of GAM.

Figure 8 shows the causal impact of TM and GAM on the particle flux Γ_r , which shows that the TM and GAM will modulate the transport as well and the influences of TM and GAM on transport are comparable except that the time scale is larger in the former case. In addition, it can also be seen that the maximum values in figure 8(a) is much smaller than that in figure 7(a), implying that the TM would mainly modulate the turbulent energy rather than the transport. The reason might be that the TM would also modify the phase between density and the potential fluctuations at the same time, which will be analyzed in detail in the future.

As the turbulent particle flux is computed as the product of root-mean square (RMS) values of density n_e^{rms} , poloidal electric field E_θ^{rms} and the coherence C_{ne} between them, it is important to give the causal relationships between TM, GAM and each flux component in order to provide a comprehensive understanding of which one would determine the transport level in the multi-scale system. According to the theory, the coherence is calculated as $C_{ne} = \frac{\Gamma_r}{n_e^{rms} E_\theta^{rms} / B_T} = \frac{\langle \tilde{n}_e \tilde{E}_\theta / B_T \rangle}{n_e^{rms} E_\theta^{rms} / B_T}$ [35]. The corresponding causal relations are shown in figure 8. It is discovered that the TM has strong impact on both n_e^{rms} and E_θ^{rms} which are of an order magnitude than that of the GAM, as can be inferred from figures 9(a1), (a2), (b1) and (b2), while their effects on the coherence do not show much large difference, as can be found in figures 9(c1) and (c2). The modulation effect of TM on turbulence is quite different from the GAM, i.e., the TM modulates the n_e^{rms} and C_{ne} on a faster time scale and the latter acts back on a longer one, whereas the interaction between TM and E_θ^{rms} shows a synchronization feature which can be clearly seen in figure 9(b1). However, for the case of GAM, it acts on both E_θ^{rms} and C_{ne} on a faster time scale and the latter

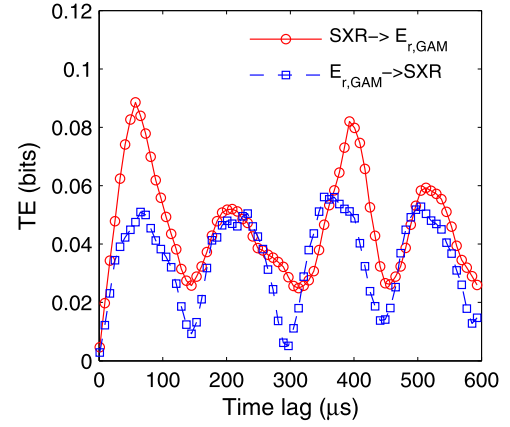


Figure 10. TE as a function of time lag between TM and GAM.

two affect the former on a longer time scale while the synchronization character is discovered in the relations between GAM and density fluctuation amplitude, as shown in figure 9(a2). From the discussions above, we can conclude that the difference in the regulation of large-scale TM and meso-scale GAM on turbulence is mainly resulted from the different modulation effect on the density fluctuation and the turbulence radial velocity ($\tilde{v}_r = \tilde{E}_\theta / B_T$). Furthermore, the causal relations show the quasi-oscillation behavior in figures 9(a2) and (c2), which seem to be coherent with the usual predator–prey models for the interaction between ZF and turbulence [4].

3.3. Causal influence of tearing mode on zonal flow dynamics

It is evident that there is also interaction between TM and GAM, as shown in figure 10. Overall, a quasi-oscillation feature is observed between them and the influence of TM on GAM is generally stronger than the backforward process, hence it can be concluded that TM has larger influence on GAM than the reverse interaction. The maximum influences occur at almost the same time lag in the two directions. Nevertheless, it is no easy to explain such an interaction as the magnetic perturbation of TM and the electrostatic potential fluctuation of GAM are not coupled directly. In order to understand the underlying physical mechanism, we have shown the relationship between TM, RS which is responsible for the GAM generation [43] and GAM for the very first time utilizing the combination of cross-conditional averaging (CCA) [44] and TE techniques. The CCA is extracted within data length larger than 50 ms in order to obtain enough samples and the density fluctuation is used as the reference signal, during which the threshold condition is selected as two times of the standard deviation, $\sigma_{CA} = 2$. The conditionally averaged TM fluctuation and RS are shown in figure 11(a1) while the RS and GAM fluctuation are plotted in figure 11(a2), while the corresponding causal relations are depicted in figures 11(b1) and (b2), respectively. It is clearly inferred that the TM modulates the RS by changing both the amplitudes of density and turbulence velocity fluctuations and the TM affects the RS on a faster time scale than the backforward reaction, leading to a limit-cycle oscillation behavior between them, as shown in

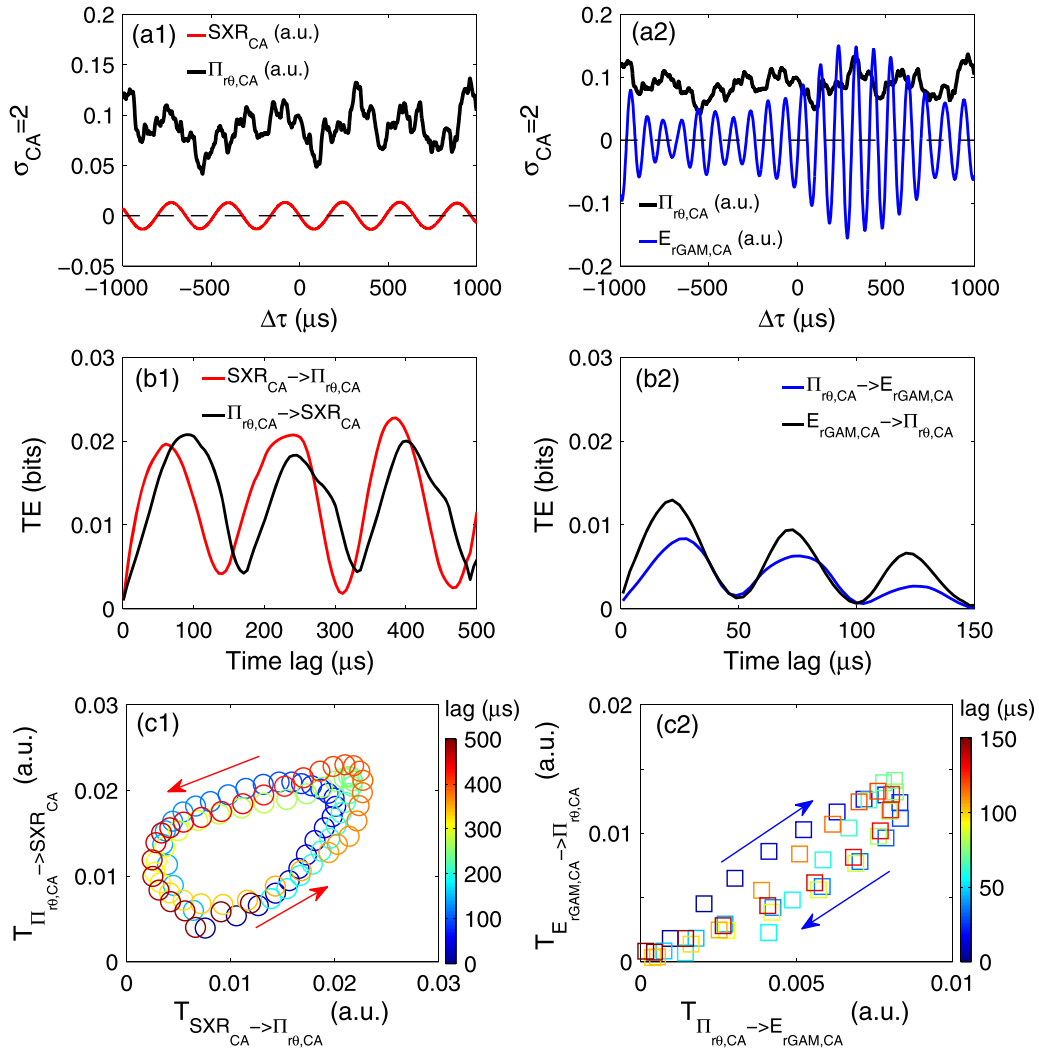


Figure 11. Conditionally averaged signals, causal relations between them and limit cycle established between the two rescaled TE values. (a1)–(c1) are the results for TM and RS while (a2)–(c2) are that for RS and GAM, respectively.

figure 11(c1). Similar limit-cycle features have also been found in the causal relations between RS and GAM, as illustrated in figure 11(c2) in addition to the fact that they would interact on a shorter time scale than that of the TM, which is supposed to be due to the fact that TM and GAM have different mode frequencies. It is also noticed that the GAM regulates the RS with both faster time scale and larger amplitude than the reverse-acting because GAM ZF modulates the turbulent velocity first, then the change in RS occurs accordingly. In addition, the causal relations between RS and GAM shows a gradual decay, which might be related to the damping nature of GAM in tokamak plasmas whereas the interaction between TM and RS is almost periodic as the amplitude of TM is kept nearly constant during the time of interest. These analyses have provided a possible explanation of the interaction between GAM and TM, i.e., the TM and GAM interact indirectly and the modulation effect of TM on GAM works through RS acting as a mediator, causing a cooperative interaction between TM and GAM as a consequence. The above results have afford a clear interpretation of the causal effects among TM, GAM dynamics and turbulence, which could also provide a guideline in understanding

the multi-scale interactions among other MHD modes such as NTMs and Alfvén modes [45], ZFs and turbulence in neutral beam heated high-performance plasmas.

4. Conclusions

In this work, multi-scale interactions among TM, GAM and turbulence in the edge plasma of the HL-2A tokamak are investigated using direct causality analysis method for the first time. Experimental results have shown that the $(m/n) = (2/1)$ TM and GAM have a modulation effect on turbulence with different spatial-temporal scales, where the former acts on the density fluctuation within the frequency range of $f = 50\text{--}150$ kHz while the GAM mainly regulates that with higher frequencies and smaller scales. There exist strong nonlinear three-wave interactions between GAM and AT. The TM has both amplitude and phase modulations whereas the GAM has only amplitude modulation effect on turbulence energy, respectively. TE analyses have indicated that both TM and GAM can modulate the turbulence energy as well as the particle transport on a faster time scale and the latter acts back on a longer time scale.

The influences of TM and GAM on transport are comparable except for that the time scale is larger in the former situation. The TM and GAM have different regulation effects on the amplitudes of density fluctuation and the turbulence radial velocity while their effects on the coherence do not show large difference. Quasi-oscillational feature is observed in the causal relations between TM and GAM and the maximum influences occur at almost the same time in both directions. Analyses have suggested the picture that the TM and GAM may interact indirectly and the modulation effect of TM on GAM is suggested to work through RS serving as a mediator, leading to a cooperative interaction between TM and GAM in the multi-scale tokamak plasma system.

Acknowledgments

We acknowledge the Center for Computational Science and Engineering of Southern University of Science and Technology for providing computational resources. This work was partly supported by National Key R & D Program of China (Grant Nos. 2019YFE03020000 and 2017YFE0301200), National Natural Science Foundation of China (Grant Nos. 11947238, 12075079, 12125502 and 11875019) and Sichuan Science and Technology Program (Grant No. 2021JDJQ0029).

ORCID iDs

J.Q. Xu  <https://orcid.org/0000-0003-4834-3005>
 J.C. Li  <https://orcid.org/0000-0001-9918-8880>
 N. Wu  <https://orcid.org/0000-0001-7949-5330>
 G.Z. Hao  <https://orcid.org/0000-0003-2310-6134>
 W. Chen  <https://orcid.org/0000-0002-9382-6295>

References

- [1] Boozer A.H. 2004 *Rev. Mod. Phys.* **76** 1071
- [2] Wesson J.A. 1978 *Nucl. Fusion* **18** 87
- [3] Horton W. 1999 *Rev. Mod. Phys.* **71** 735
- [4] Diamond P.H., Itoh S.-I., Itoh K. and Hahm T.S. 2005 *Plasma Phys. Control. Fusion* **47** R35
- [5] Fujisawa A. et al 2004 *Phys. Rev. Lett.* **93** 165002
- [6] Conway G.D., Smolyakov A.I. and Ido T. 2022 *Nucl. Fusion* **62** 013001
- [7] Lin Z., Hahm T.S., Lee W.W., Tang W.M. and White R.B. 1998 *Science* **281** 1835
- [8] Shats M.G. and Solomon W.M. 2002 *Phys. Rev. Lett.* **88** 045001
- [9] Birkenmeier G., Ramisch M., Schmid B. and Stroth U. 2013 *Phys. Rev. Lett.* **110** 145004
- [10] Furth H.P., Killeen J. and Rosenbluth M.N. 1963 *Phys. Fluids* **6** 459
- [11] La Haye R.J. 2006 *Phys. Plasmas* **13** 055501
- [12] Doyle E.J. et al 2007 Progress in the ITER physics basis chapter 2: plasma confinement and transport *Nucl. Fusion* **47** S18
- [13] Waelbroeck F.L. 2009 *Nucl. Fusion* **49** 104025
- [14] Ishizawa A., Kishimoto Y. and Nakamura Y. 2019 *Plasma Phys. Control. Fusion* **61** 054006
- [15] Choi M.J. 2021 *Rev. Mod. Plasma Phys.* **5** 9
- [16] Bardóczi L., Rhodes T.L., Carter T.A., Navarro A.B., Peebles W.A., Jenko F. and McKee G. 2016 *Phys. Rev. Lett.* **116** 215001
- [17] Bardóczi L. et al 2017 *Phys. Plasmas* **24** 056106
- [18] Choi M.J. et al 2017 *Nucl. Fusion* **57** 126058
- [19] Sun P.J. et al 2018 *Plasma Phys. Control. Fusion* **60** 025019
- [20] Estrada T., Ascasíbar E., Blanco E., Cappa A., Hidalgo C., Ida K., López-Fraguas A. and van Milligen B.P. 2016 *Nucl. Fusion* **56** 026011
- [21] Ida K. et al 2001 *Phys. Rev. Lett.* **88** 015002
- [22] Jiang M. et al 2018 *Nucl. Fusion* **58** 026002
- [23] Jiang M. et al 2019 *Nucl. Fusion* **59** 066019
- [24] Romanelli F. 1989 *Phys. Fluids B* **1** 1018
- [25] Xu J.Q. et al 2022 *Phys. Plasmas* **29** 012508
- [26] Ishizawa A. and Nakajima N. 2007 *Phys. Plasmas* **14** 040702
- [27] Amblard P.-O. and Michel O. 2013 *Entropy* **15** 113
- [28] Xu M. et al 2019 *Nucl. Fusion* **59** 112017
- [29] Zhao K.J. et al 2006 *Phys. Rev. Lett.* **96** 255004
- [30] Cheng J. et al 2013 *Phys. Rev. Lett.* **110** 265002
- [31] Schreiber T. 2000 *Phys. Rev. Lett.* **85** 461
- [32] van Milligen B.P., Birkenmeier G., Ramisch M., Estrada T., Hidalgo C. and Alonso A. 2014 *Nucl. Fusion* **54** 023011
- [33] Wibrall M., Pampu N., Priesemann V., Siebenhühner F., Seiwert H., Lindner M., Lizier J.T. and Vicente R. 2013 *PLoS One* **8** e55809
- [34] Shi Z.B. et al 2014 *Rev. Sci. Instrum.* **85** 023510
- [35] Hidalgo C. 1995 *Plasma Phys. Control. Fusion* **37** A53
- [36] Beall J.M., Kim Y.C. and Powers E.J. 1982 *J. Appl. Phys.* **53** 3933
- [37] Mahdizadeh N., Greiner F., Ramisch M., Stroth U., Guttenfelder W., Lechte C. and Rahbarnia K. 2005 *Plasma Phys. Control. Fusion* **47** 569
- [38] Lan T. et al 2008 *Plasma Phys. Control. Fusion* **50** 045002
- [39] Zhong W.L. et al 2015 *Nucl. Fusion* **55** 113005
- [40] van Milligen B.P., Sánchez E., Estrada T., Hidalgo C., Brañas B., Carreras B. and García L. 1995 *Phys. Plasmas* **2** 3017
- [41] Bardóczi L., Logan N.C. and Strait E.J. 2021 *Phys. Rev. Lett.* **127** 055002
- [42] Choi M.J. et al 2021 *Nat. Commun.* **12** 375
- [43] Diamond P.H. and Kim Y.B. 1991 *Phys. Fluids B* **3** 1626
- [44] Teliban I., Block D., Piel A. and Greiner F. 2007 *Plasma Phys. Control. Fusion* **49** 485
- [45] Chen L. and Zonca F. 2016 *Rev. Mod. Phys.* **88** 015008